Earth and Planetary Science Letters 351-352 (2012) 247–257 (reprint)

Contents lists available at SciVerse ScienceDirect

Earth and Planetary Science Letters

journal homepage: www.elsevier.com/locate/epsl

The 2012 Sumatra great earthquake sequence

Zacharie Duputel [a,*], Hiroo Kanamori [a], Victor C. Tsai [a], Luis Rivera [b], Lingsen Meng [a], Jean-Paul Ampuero [a], Joann M. Stock [a]

[a] Seismological Laboratory, California Institute of Technology, 1200 E. California Blvd., Pasadena, CA 91125, USA
[b] IPGS-EOST, CNRS/Université de Strasbourg, UMR 7516, 5 rue René Descartes, 67084 Strasbourg Cedex, France

ARTICLE INFO

Article history:
Accepted 15 July 2012
Editor: P. Shearer

Keywords:
2012 Sumatra earthquake sequence
intraplate earthquakes
earthquake source observations
seismicity and tectonics
surface waves and free oscillations

ABSTRACT

The equatorial Indian Ocean is a well known place of active intraplate deformation defying the conventional view of rigid plates separated by narrow boundaries where deformation is confined. On 11 April 2012, this region was hit in a couple of hours by two of the largest strike-slip earthquakes ever recorded (moment magnitudes Mw=8.6 and 8.2). Broadband seismological observations of the Mw=8.6 mainshock indicate a large centroid depth (~30 km) and remarkable rupture complexity. Detailed study of the surface-wave directivity and moment rate functions clearly indicates the partition of the rupture into at least two distinct subevents. To account for these observations, we developed a procedure to invert for multiple-point-source parameters. The optimum source model at long period consists of two point sources separated by about 209 km with magnitudes Mw=8.5 and 8.3. To explain the remaining discrepancies between predicted and observed surface waves, we can refine this model by adding directivity along the WNW–ESE axis. However, we do not exclude more complicated models. To analyze the Mw=8.2 aftershock, we removed the perturbation due to large surface-wave arrivals of the Mw=8.6 mainshock by subtracting the corresponding synthetics computed for the two-subevent model. Analysis of the surface-wave amplitudes suggests that the Mw=8.2 aftershock had a large centroid depth between 30 km and 40 km. This major earthquake sequence brings a new perspective to the seismotectonics of the equatorial Indian Ocean and reveals active deep lithospheric deformation.

1. Introduction

Great strike-slip earthquakes are very uncommon, with the most well-known recent events being the Mw=7.8 2001 Kunlun earthquake, the Mw=7.9 2002 Denali earthquake and the Mw=8.1 2004 Macquarie Island earthquake (Tsuboi et al., 2003; Tocheport et al., 2006; Hayes et al., 2009a; Duputel et al., 2012). Other large events are also reported in the first half of the 20th century, including the two major M~8.0 1905 Mongolian earthquakes and the Ms=8.6 1950 Assam earthquake, although details of their source characteristics are not known due to the small number of observations (Ben-Menahem et al., 1974; Chen and Molnar, 1977; Okal, 1977; Schlupp and Cisternas, 2007). Yet it is known that many large strike-slip earthquakes involve remarkable rupture complexity, and the Mw=8.1 1998 Balleny islands earthquake (Hjörleifsdóttir et al., 2009) serves as a good example of this. The seismic data from this event can be explained by subevents with different mechanisms (Henry et al., 2000). Rupture branching onto multiple subfaults was also observed, for example, during the Mw=7.3 1992 Landers earthquake, during the Mw=7.8 2001 Kunlun earthquake (Tocheport et al., 2006) and, more recently, during the Mw=7.2 2010 El Mayor–Cucapah earthquake (Hauksson et al., 2011).

The 2012 Sumatra great earthquake sequence is particularly interesting for several reasons. First, with moment magnitudes Mw ≥ 8.2, it consists of two of the largest strike-slip earthquakes ever recorded, and is among the largest intraplate earthquakes on instrumental records. Secondly, this unusual series of large intraplate earthquakes occurred in the oceanic lithosphere of the Cocos Basin (equatorial Indian Ocean), which has a unique seismotectonic environment. This region is bounded by the Sunda Megathrust to the north, the Wharton Basin to the south, the Ninetyeast Ridge to the west and the Investigator Fracture Zone to the east (Fig. 1). The whole area constitutes a diffuse deformation zone which is currently interpreted as the boundary separating the Indian and Australian Plates (Wiens et al., 1985; Deplus et al., 1998; Delescluse and Chamot-Rooke, 2007; DeMets et al., 2010). The 2012 Sumatra earthquake sequence began on 11 April 2012, when the Mw=8.6 Sumatra event occurred off the west coast of Northern Sumatra (8 h 38 min 37 s UTC—zero time used from here, 2.31°N, 93.06°E; U. S. Geological Survey—USGS), about 400 km southwest of Aceh (Fig. 1). Another major Mw=8.2 earthquake occurred 2 h after the mainshock (10 h 43 min 9 s UTC, 0.77°N, 92.45°E; USGS), approximately 200 km to the south. These earthquakes were preceded by a Mw=7.3 earthquake on 10 January 2012, located very close to the epicenter of the mainshock.

* Corresponding author. Tel.: +1 626 395 3801.
E-mail address: zacharie@gps.caltech.edu (Z. Duputel).

0012-821X/$ - see front matter © 2012 Elsevier B.V. All rights reserved.
http://dx.doi.org/10.1016/j.epsl.2012.07.017

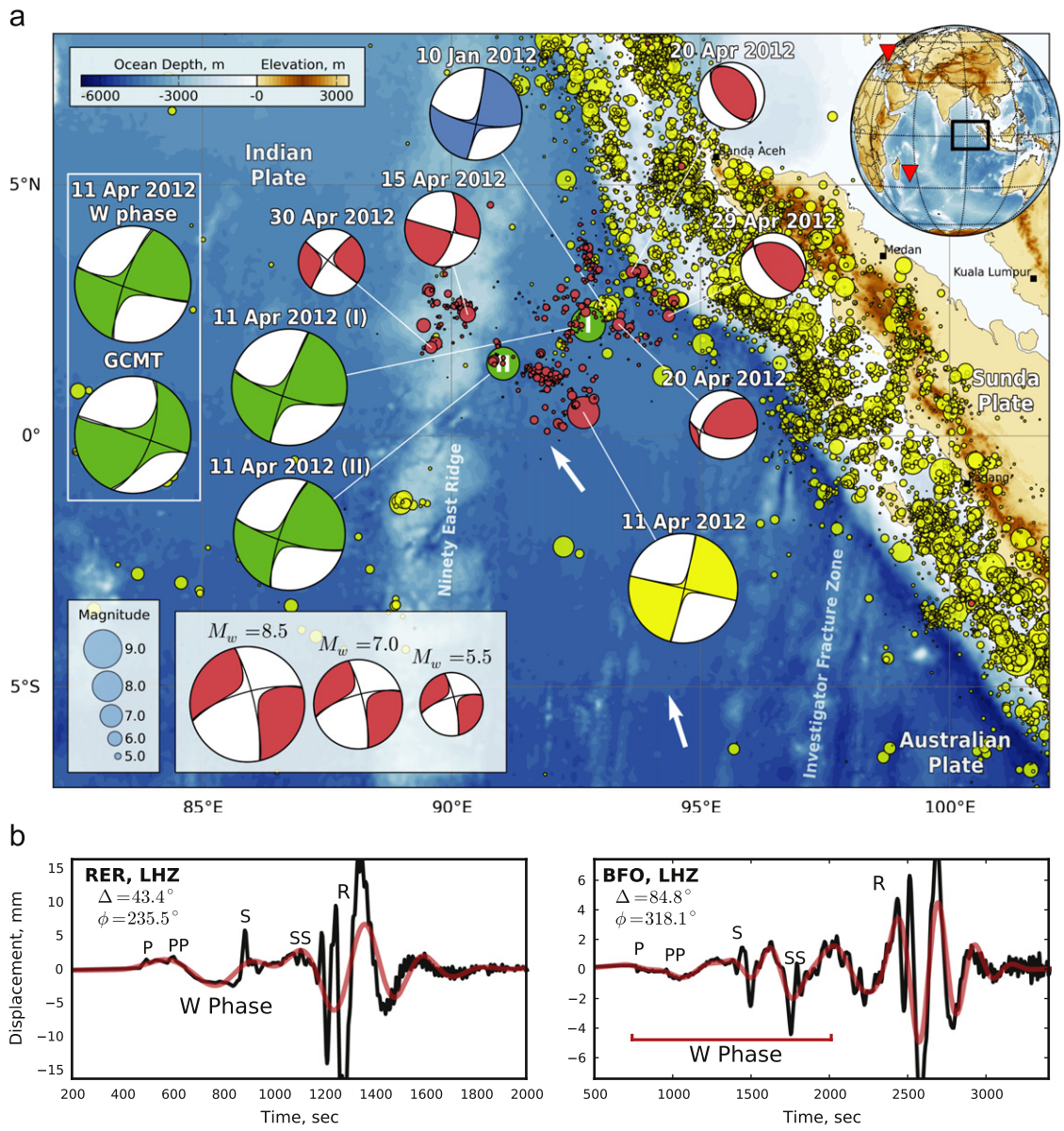

Fig. 1. The 2012 Sumatra great earthquake sequence. (a) Map of the 2012 Sumatra great earthquake region. The 11 April 2012 mainshock can be decomposed into two subevents separated by about 200 km (green mechanisms and circles labeled I and II). The W phase and Global CMT (GCMT solution available in July 2012; Ekström et al., 2012.) single-point-source solutions for the mainshock (inset green mechanisms), the W phase solutions for the 10 January foreshock (blue mechanism), for the Mw=8.2 aftershock (yellow mechanism) and for the $5.8 \leq Mw < 8.2$ aftershocks (red mechanisms) are shown. Yellow circles indicate the earthquake epicenters and magnitudes from the National Earthquake Information Center (NEIC) catalog between 1 January 1973 and 10 April 2012. Red circles show the events since the Mw=8.6 11 April 2012 earthquake through May 2012. White arrows indicate the direction of motion of the Australian plate relative to the Indian plate at about 13 mm/yr (DeMets et al., 2010). The red triangles on the globe indicate the locations of broadband stations RER and BFO. (b) W phase waveforms recorded at station RER (epicentral distance Δ=43°, azimuth ϕ=235°) and BFO (Δ=84°, ϕ=317°) during the 11 Mw=8.6 April 2012 Sumatra earthquake. In each figure, the black trace is the vertical broad-band displacement data and the red trace is the very-long-period displacement data filtered in the 200–1000 s passband. The W phase, body wave arrivals (P, PP, S, SS) and the Rayleigh wave train (R) are indicated.

The complexity of the Mw=8.6 Sumatra earthquake was detected early on by preliminary source analyses (Hayes, 2012; Kiser and Ishii, 2012; Meng et al., 2012; Shao et al., 2012; Wei, 2012). The intricate distribution of aftershocks, the complexity of short-period body-wave waveforms and the remoteness of geodetic instruments due to the oceanic epicenter location make it difficult to resolve the rupture process in detail. On the other hand, seismic waves from the 2012 Sumatra earthquake sequence were recorded by hundreds of global broadband seismographs, enabling robust characterization of the overall rupture characteristics at long period. The goal of this work is to provide a reliable description of the first-order source attributes of the mainshock and its aftershocks using long-period (100–500 s) and ultra-long-period (>500 s) data. In the following, we analyze this complicated earthquake sequence using both single-point-source characterization and multiple-point-source inversion. This enables us to resolve distinct aspects of the mainshock rupture process.

2. W phase inversion for point-source geometry

Great earthquakes ($Mw > 8.0$) generally involve rupture propagation over large distances in a few minutes. In such cases, the point-source approximation is only valid for ultra-long-period seismic waves such as the W phase, which corresponds to the superposition of the first overtones of the Earth normal modes

between 100 s and 1000 s (Kanamori, 1993). As shown in Fig. 1b, the W phase is conspicuous between the P wave and the surface wave train on broadband displacement records of the Mw=8.6 2012 Sumatra earthquake. The W phase source-inversion algorithm was initially developed to provide rapid characterization of the seismic source for tsunami warning purposes (Kanamori and Rivera, 2008; Hayes et al., 2009b; Duputel et al., 2011) and is a reliable and straightforward method to resolve the first-order attributes of large earthquakes (Tsai et al., 2011; Duputel et al., 2012). Point-source parameters of all events with Mw $\geq$ 5.8 during the 2012 Sumatra earthquake sequence were inverted using the W phase algorithm. The deviatoric moment tensor components as well as the centroid locations (latitudes, longitudes, depths) and timings were resolved following the procedure described by Duputel et al. (2012). The W phase solutions obtained in this study are presented in Fig. 1a.

For the Mw=8.6 mainshock, we inverted records of 66 broadband stations within an epicentral distance of 90° for a point-source moment tensor. Most of the 113 selected channels are from ultra-long-period seismometers (STS-1) with low noise level in the 200–1000 s passband used for the inversion. The solution is shown in Fig. 1 (inset green mechanism) and examples of waveform fits are included in the Supplementary material (Fig. S1). The scalar moment is estimated to be $M_0=9.2\times10^{21}$ N m (Mw=8.6) and the best double-couple nodal planes have orientations given by strike $\phi=199°$, dip $\delta=78°$, rake $\lambda=7°$ (NNE–SSW plane) and $\phi=108°$, $\delta=83°$, $\lambda=168°$ (WNW–ESE plane). The moment tensor thus determined has a relatively small intermediate eigenvalue (eigenvalues are $\lambda_1=8.74$, $\lambda_2=0.89$ and $\lambda_3=-9.63$ in units of 10^{28} N m, $\varepsilon=-\lambda_2/\max(|\lambda_1|,|\lambda_3|)=-0.09$) compared to the Global CMT solution available in July 2012 ($\lambda_1=8.10$, $\lambda_2=1.71$ and $\lambda_3=-9.81$ in units of 10^{28} N m, $\varepsilon=-0.17$), which was obtained using mantle waves with periods shorter than 200 s. Although the W phase solution does not indicate any apparent complexity at ultra-long period (200–1000 s), the larger non-double-couple component in the Global CMT solution suggests a complicated rupture process at shorter periods for the mainshock.

Source analysis of the Mw=8.2 aftershock is more complicated since long-period waveforms are disturbed by the large amplitude arrivals of the Mw=8.6 mainshock, which occurred about 2 h before. To handle this, we generated a residual trace by subtracting the synthetics for the mainshock from the data. Since the disturbances mostly correspond to R2, G2 and G3 wavetrains that are sensitive to shallow lateral heterogeneities, the synthetics are computed using the spectral-element method (SEM, Komatitsch and Tromp, 1999) for a 3D Earth model composed of the mantle model S362ANI (Kustowski et al., 2008) and the crustal model Crust 2.0 (Bassin et al., 2000). To account for the source complexity of the mainshock, we used the two-point-source model presented in Section 5. We then inverted for a point-source moment tensor using the residuals between observed seismograms and SEM synthetics in the 120–600 s passband as the data vector. The solution shown in Fig. 1 (yellow mechanism) was obtained using 26 stations with a well-balanced azimuthal distribution for which examples of waveform fit are shown in Fig. S2. This inversion also yielded a small intermediate eigenvalue (eigenvalues are $\lambda_1=2.28$, $\lambda_2=0.07$ and $\lambda_3=-2.35$ in units of 10^{28} N m, $\varepsilon=-0.03$). The scalar moment is $M_0=2.5\times10^{21}$ N m (Mw=8.2) and the best double-couple nodal planes have orientations $\phi=13°$, $\delta=86°$, $\lambda=-1°$ (NNE–SSW plane) and $\phi=104°$, $\delta=89°$, $\lambda=-176°$ (WNW–ESE plane).

We also performed point-source inversions to determine the moment tensor of the 10 January foreshock (blue mechanism in Fig. 1) and of the 5.8 $\leq$ Mw < 8.2 aftershocks through May 2012 (red mechanisms). Following the strategy of Hayes et al. (2009b), the passband is gradually shifted toward higher frequencies for smaller earthquakes to reduce the effect of the long-period background noise (cf., Duputel et al., 2012). The W phase solutions are in overall good agreement with the Global CMT and USGS CMT solutions. They all indicate strike-slip earthquakes except for two Mw=5.8 thrust events that occurred near the Sunda trench on 20 April 2012 and 29 April 2012. It is difficult to infer anything about the mainshock rupture orientation from these results. From the NNE–SSW trends of the Ninetyeast ridge and fracture zones in the Cocos Basin, one might guess a similar orientation for the main rupture. This assumption is reasonable in view of the centroid location of the Mw=8.2 event with respect to the Mw=8.6 mainshock, but seems in contradiction with the many aftershocks located at the western margin of the basin, including the Mw=6.2 earthquake on 15 April 2012 and the Mw=5.8 earthquake on 30 April 2012.

3. Surface-wave directivity and radiation pattern

The true fault plane orientation of the Mw=8.6 2012 Sumatra earthquake is unclear. Preliminary finite fault inversions fail to discriminate which nodal plane corresponds to the fault and the complex distribution of aftershocks presented in Fig. 1 (also shown in Fig. S3 in the Supplementary material) indicates two major parallel WNW–ESE lineations separated by ~150 km and at least one additional orthogonal NNE–SSW trend. For large earthquakes, long-period surface waves can provide useful information on the source finiteness and rupture directivity.

To investigate the possible directivity effects of the Mw=8.6 mainshock, seismograms were equalized to an epicentral distance of $\Delta_0=90°$ using the procedure described by Kanamori (1970). To do this, we retrieve the wavefield $U(\omega,\Delta_0,\varphi)$ at distance Δ_0 and azimuth φ from the observations at distance Δ using

$$U(\omega,\Delta_0,\varphi)=\left(\frac{\sin\Delta}{\sin\Delta_0}\right)^{1/2}U(\omega,\Delta,\varphi)\exp\left[i\left(\frac{\omega a(\Delta-\Delta_0)}{c}-\frac{m\pi}{2}\right)\right]\exp\left[k(\Delta-\Delta_0)\right] \quad (1)$$

where m is the number of epicentral or antipodal passages in going from Δ to Δ_0, and c and κ are respectively the phase velocity and attenuation coefficient as a function of frequency. This operation ideally removes the differences in propagation effects for different stations, so the amplitude as a function of azimuth should reflect the source's radiation pattern. The values of c and κ used for the equalization of the fundamental Love and Rayleigh waves are from the PREM model (Dziewonski and Anderson, 1981). We exploited both the short arc (R1, G1) and the long arc (R2, G2) wave trains to improve the azimuthal coverage and measured root mean square (rms) amplitudes of equalized seismograms in the 100–400 s passband. The result, presented as inset circular plots in Fig. 2a and b and in Figs. S4–S5 in the Supplementary material, shows quite simple radiation patterns with deep (i.e., small amplitude) nodes and a clear asymmetry suggesting directivity in the southwest direction.

To further analyze this apparent directivity, we measured the ratio between observed and predicted surface-wave amplitudes in the 200–400 s passband. To remove the effect of the mechanism, dispersion and attenuation, we used single-point-source synthetic seismograms computed with the SEM method for a 3D Earth model composed of the models S362ANI and Crust 2.0. We focus here on the variation of the amplitude ratio (observed/predicted) as a function of azimuth. The point-source solution indicates a strike-slip mechanism, which produces four-lobed surface-wave radiation patterns with different orientations for Love and Rayleigh waves (cf., inset circular plots in Fig. 2a and b). Small amplitudes (and thus smaller signal-to-noise ratios) are expected in the nodal azimuths of the surface-wave radiation patterns. We thus considered both

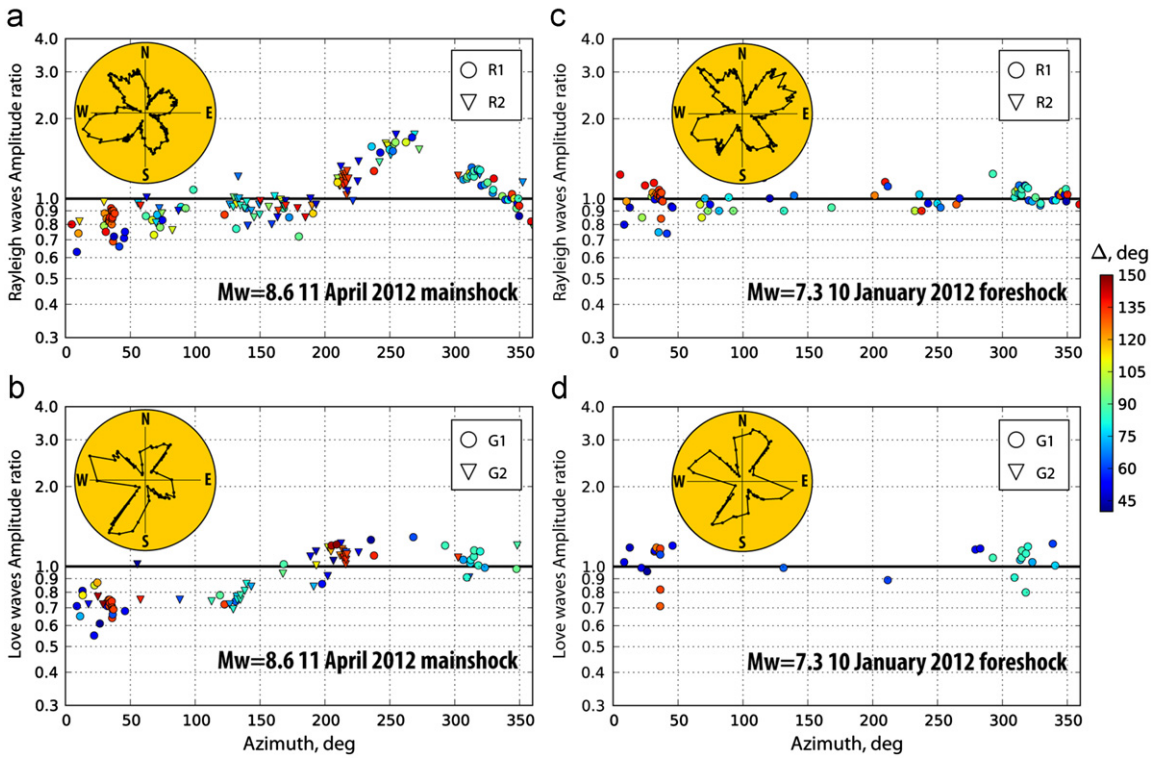

Fig. 2. Long-period surface-wave directivity for the Mw=8.6 11 April 2012 Sumatra earthquake and for the Mw=7.3 10 January foreshock. Ratios between observed and predicted rms amplitudes have been measured in the 200–400 s passband. (a, b) Amplitude ratios for the Mw=8.6 mainshock. (c, d) Amplitude ratio measured during the Mw=7.3 foreshock. (a, c) Ratios for Rayleigh R1 and R2 wave trains. (b, d) Ratios for Love G1 and G2 wave trains. Short and long arc wave trains are presented respectively using circles and triangles colored as a function of epicentral distance (Δ). Azimuthal variation of amplitude ratios is larger for Rayleigh waves because of their smaller phase velocity, closer to typical rupture speeds, which enhances their sensitivity to rupture directivity. Inset diagrams are equalized Rayleigh and Love waves in the 100–400 s passband. (For interpretation of the references to color in this figure legend, the reader is referred to the web version of this article.)

Rayleigh and Love waves which bring complementary information; we used minor-arc (R1, G1) as well as major-arc (R2, G2) wave trains to improve the azimuthal coverage of the radiation patterns. If there were no effect of finiteness, the observed/predicted amplitude ratios would be unity for all azimuths. For the Mw=8.6 2012 Sumatra earthquake, we clearly see in Fig. 2a and b that the Rayleigh- and Love-wave amplitudes are enhanced in azimuths around 260°N (i.e., 260° clockwise from north).

This directivity toward 260°N is not expected for rupture propagation along the NNE–SSW or WNW–ESE nodal plane of the W phase or Global CMT point-source solutions. This suggests geometric complexity of faulting or possible bias due to structural heterogeneities unaccounted for in the considered 3D Earth model. To test the validity of our amplitude ratio observations, we made the same measurements for the Mw=7.3 10 January 2012 Sumatra foreshock for which the W phase solution also indicates a strike-slip mechanism (blue mechanism in Fig. 1). Fig. 2c and d show no anomalous azimuthal variations of the amplitude ratio and indicate that the observed directivity patterns for the April 11 event are due to source effects.

We also computed equalized seismograms and observed/predicted amplitude ratios for the Mw=8.2 aftershock. As for the moment tensor calculation presented in Section 2, we used a residual trace by subtracting the synthetics for the mainshock from the data in order to remove the long-period disturbances generated by the Mw=8.6 mainshock. The equalization diagram and amplitude ratios for the Mw=8.2 aftershock are presented in Figs. S6 and S7 in the Supplementary material. The rupture orientation is difficult to infer here since there is no obvious directivity visible on the equalized seismograms and on the observed/predicted amplitude ratios. The surface-wave radiation diagram is remarkably simple which suggests a simpler rupture than that of the Mw=8.6 mainshock.

4. Surface-wave moment rate functions

To further investigate the directivity and complexity of the Mw=8.6 11 April 2012 earthquake, we computed broadband (periods of 25–600 s) minor-arc (R1) Rayleigh-wave moment rate functions (MRFs). We removed the dispersive wave propagation effects by deconvolving the data by point-source synthetic seismograms computed for the Global CMT solution. We chose to use this solution instead of the W phase CMT solution since the Global CMT synthetics better fit the Rayleigh waves in the 25–600 s passband. An alternative approach would be to use waveforms of the Mw=7.3 10 January foreshock as an empirical Green's function. This technique, however, is limited at long period by the background noise level, which can be large for a Mw=7.3 earthquake, and at short period by the possible complexity of the moment rate function of the foreshock. Such an empirical Green's function approach also has complications due to differences in locations and focal mechanisms of the two events. To take into account the effect of lateral structural variations, we used SEM synthetics computed for a 3D Earth model (S362ANI and Crust2.0). We used the projected Landweber deconvolution method (Bertero et al., 1999; Lanza et al., 1999) imposing causality, positivity and a maximum rupture duration of 200 s. The R1 MRFs are shown in Fig. 3 as a function of the directivity parameter (Ruff, 1984; Ammon et al., 2006), with the assumption of directivity toward 250°N, which allows optimal alignment of the MRFs. Similar plots assuming rupture directivity toward 235°N and 265°N are shown for comparison in the Supplementary material (Figs. S8 and S9). This operation allows us to transform any cosine azimuthal moveout into a linear moveout. The directivity effect revealed by surface-wave amplitudes is also visible here. The MRFs have large amplitudes and short durations in the southwest direction and the

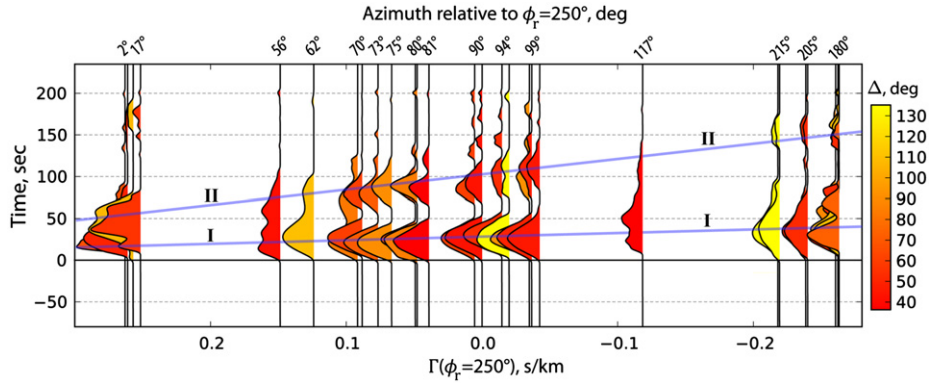

Fig. 3. Rayleigh wave MRFs for the Mw=8.6 11 April 2012 Sumatra earthquake. The R1 MRFs obtained using the projected Landweber method are ordered as a function of the directivity parameter $\Gamma=\cos(\phi-\phi_r)/c$, where ϕ is the azimuth of the station from the epicenter, ϕ_r is the rupture direction and c is the phase velocity (here we assume $\phi_r=250^\circ$ and $c=3.8$ km/s). The equivalent azimuth relative to $\phi_r=250^\circ$ is indicated for groups of stations along the top axis. The positive amplitudes are colored as a function of epicentral distance (Δ). The durations of MRFs systematically increase from 80 s to about 170 s as Γ decreases from left to right. Blue lines I and II identify discrete pulses that are visible on several MRFs. (For interpretation of the references to color in this figure legend, the reader is referred to the web version of this article.)

total duration increases with decreasing directivity parameter. We also found clear evidence of radiation complexity. As the azimuth relative to the direction 250°N increases, a strong second pulse shifts systematically to later times. The linear moveout of this second pulse suggests rupture partitioning into at least two distinct subevents, possibly aligned along an azimuth of about 250°N with respect to the Global CMT centroid location. Other side lobes are observed around 70 s for a relative azimuth of 180° and around 170 s for azimuths between 2° and 17°. However, because of their relatively small amplitudes, it is difficult to associate them to particular rupture features.

5. Multiple-point-source analysis

To account for the R1 MRFs observations that suggest two distinct subevents for the Mw=8.6 mainshock, we performed a multiple-point-source inversion. We simultaneously inverted the long-period data for the subevent moment tensors, locations (latitudes, longitudes, depths), time delays and half durations using a modified version of the Neighborhood Algorithm sampler (NA, Sambridge, 1999). The inversion is performed using the W phase at shorter periods than is typically used for our single-point-source inversions of Mw > 8.0 earthquakes, to better characterize the complexity of the rupture. This method has been validated with several synthetic tests and the same approach has been successfully applied to the 2009 Samoa earthquake (cf. Fig. S10 in the Supplementary material). We discuss here the solutions obtained using the 150–500 s passband.

Our preferred two-point-source model is included in Fig. 1 as the green mechanisms and circles labeled I (first subevent) and II (second subevent). The 10,200 locations in time and space explored after 50 NA iterations are shown by circles in Fig. 4. Using the two distinct pulses observed on the R1 MRFs (Fig. 3) for guidance, the point-source delays were sampled from 10 s to 40 s for the first subevent and from 50 s to 120 s for the second subevent. Following the NA procedure, higher sampling is made in regions associated with smaller misfits, revealing two distinct clouds around the optimum locations for each subevent. Although only W phase waveforms were used in the inversion, the waveform fits of the surface waves are significantly improved using the two-point-source model, as shown in Fig. 5. A systematic comparison between predicted waveforms and observed seismograms is shown in the Supplementary material (Figs. S11–S14).

The first subevent has a centroid time delay of 36 s with respect to the origin time and a moment of $M_0=8.0\times10^{21}$ N m (Mw=8.5) that represents almost 70% of the total moment. It is located very close to the single-point-source location inferred from W phase and Global CMT results (2.22°N, 92.74°E). The second subevent has a centroid time delay of 106 s, with a smaller scalar moment $M_0=3.7\times10^{21}$ N m (Mw=8.3), and is located ~200 km southwest of the first subevent (1.44°N, 91.04°E; see Fig. 1). The half durations for the first and second sources are estimated to be 43 s and 70 s, respectively. This parameter is poorly constrained by the inversion due to the long periods of the analyzed seismic waves.

6. Centroid depth

As shown in Fig. 6a and b, with the relative size and spatial and temporal distribution of the two point sources used to describe the mainshock rupture, the computed radiation patterns can reproduce the overall directivity toward 260°N shown in Fig. 2a and b. We can now use this model to determine a range of reasonable centroid depths for the mainshock. Since there is almost no depth dependence of sensitivity kernels for Love waves, we show the result for Rayleigh waves (more details are provided in the Supplementary material). Fig. 7 compares the amplitudes of the observed Rayleigh waves in the 200–600 s passband with those of the two-point-source synthetics computed for depths from 10 to 60 km. The synthetics are computed using SEM for a 3D Earth model combining S362ANI and Crust 2.0, with a Moho depth of less than 10 km in the source region. It is clear that the centroid depth of 30 km can best explain observed amplitudes (since the best-fit line to the observed and predicted amplitudes – in red – most closely matches a 1:1 relationship shown with a dashed line). Thus, the two-point-source model shown in Fig. 4 with a centroid depth of 30 km is the long-period source model for the Mw=8.6 11 April Sumatra earthquake that is constrained most objectively by the data.

We performed the same analysis to estimate the centroid depth of the Mw=8.2 aftershock. To eliminate the disturbances caused by the long-period surface-wave arrivals of the Mw=8.6 mainshock, we substracted the SEM synthetics for the two-point-source model from the data and used a shorter period passband (100–400 s). Fig. 8 compares the observed Rayleigh wave amplitudes with those of the SEM synthetics computed at different depths for the single-point-source model presented in Section 2 for the Mw=8.2 aftershock. This analysis suggests that the Mw=8.2 11 April Sumatra earthquake occurred at a depth similar to the Mw=8.6 mainshock, since the observed amplitudes are best explained by centroid depths around 30–40 km.

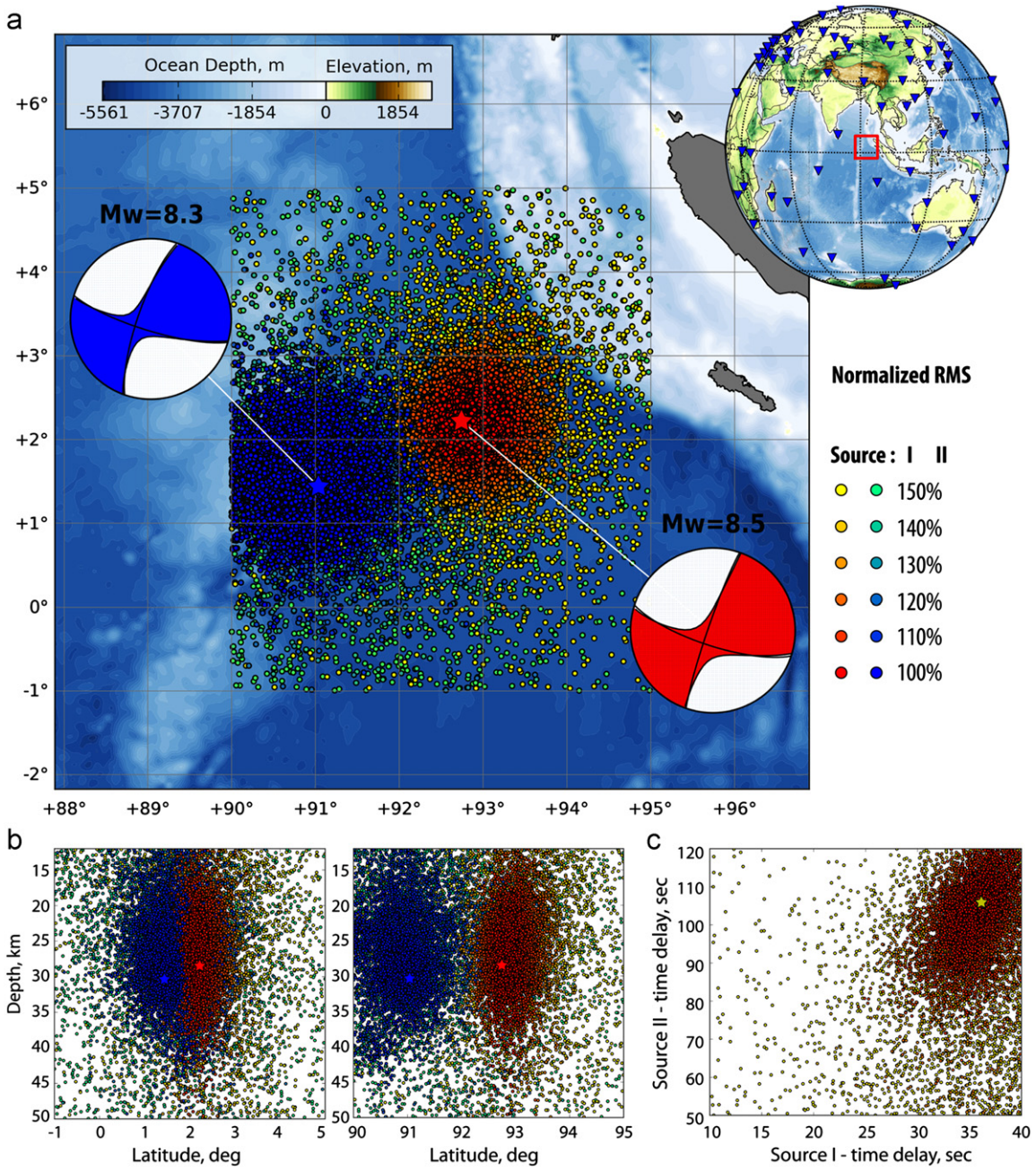

Fig. 4. Multiple-point-source inversion result for the Mw=8.6 2012 Sumatra earthquake. Circles show explored locations in time and space using a modified version of the Neighborhood Algorithm sampler (NA, Sambridge, 1999). Their colors indicate the rms misfit normalized by their minimum (i.e., red–yellow colormap for source I and blue–green colormap for source II). (a) Explored latitudes and longitudes. Used stations are indicated by blue triangles on the globe. (b) Explored latitudes and longitudes as a function of explored depths. Explored locations are shown in red for source I (first subevent) and in blue for source II (second subevent). The red and blue stars indicate the corresponding optimum locations. (c) Explored point-source delays for source II (second subevent) as a function of explored point-source delay for source I (first subevent). The colormap used in c corresponds to the colormap of source I in a and b. (For interpretation of the references to color in this figure legend, the reader is referred to the web version of this article.)

7. First-order determination of fault planes

The two-point-source model presented so far for the Mw=8.6 mainshock is a robust result and requires virtually no assumptions. However, we can refine our model results by making a few reasonable assumptions. The surface-wave radiation patterns shown in Fig. 6b suggest that slightly stronger directivity toward 260°N would improve the match between the observed and computed radiation patterns of both Love and Rayleigh waves. Since in the previous analysis the temporal finiteness for each of the two point sources is modeled by a single MRF for all stations (i.e., an isosceles triangle), the only directivity for such a model comes from the relative offset of the two subevents in space and time. A simple way to improve the directivity fit toward 260°N is to replace the isosceles MRF by an azimuthally dependent MRF of an asymmetric bilateral rupture using a source finiteness function of the type introduced by Ben-Menahem (1961) and Haskell (1963). The parameters involved are $L1$, fault length in the rupture direction; $L2$, fault length in the opposite direction; V, rupture speed; and τ, the local rise time. We assume that the slip distribution is uniform, $V=1.8$ km/s, and $\tau=25$ s. The rupture velocity was chosen to agree with preliminary finite-fault inversion results (Hayes, 2012; Shao et al., 2012; Wei,

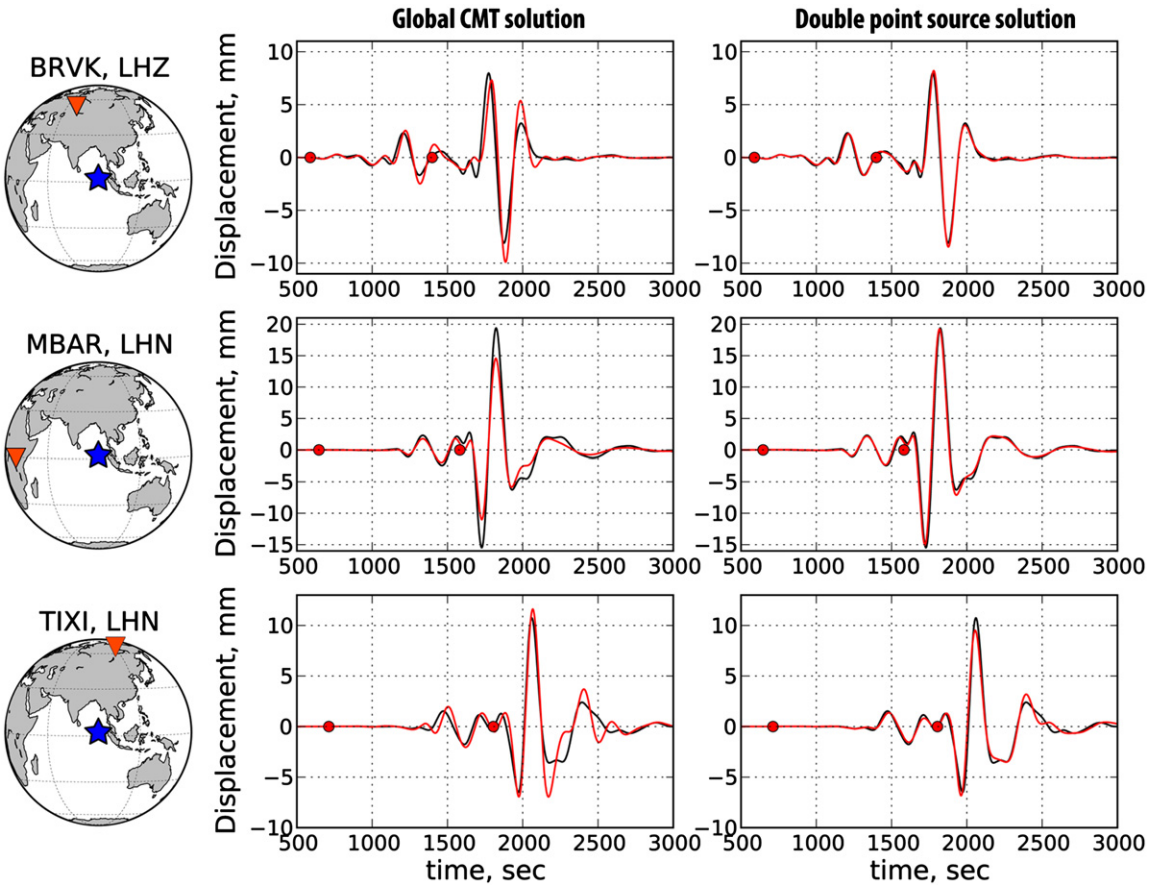

Fig. 5. Waveform fit for single- and double-point-source models. Long-period (150–500 s) surface wave motions at stations BRVK, MBAR and TIXI (black traces) are compared to predictions for the Global CMT simple point-source solution (red traces, on left) and for the two-subevent model (red traces, on right). The waveform segments used in the multiple point source inversion are bounded by red dots. (For interpretation of the references to color in this figure legend, the reader is referred to the web version of this article.)

2012; Yue et al., in press). The relatively large τ assumed here reflects the large amount of slip resulting from the large moment and the relatively small source dimension. Our objective is to make a slight modification of the two-point-source model to better match the observed radiation patterns using a model of simple asymmetric bilateral faulting. We gridsearched for an optimum faulting orientation (assuming the two possible fault strikes for each mechanism) and rupture propagation lengths, $L1$ and $L2$. The explored parameters and the corresponding rms misfit values are shown in Fig. S18. The optimum model shown in Fig. 6c corresponds to two WNW–ESE parallel bilateral faults. Although the optimum model shows asymmetric ruptures with a predominant propagation in the 288°N direction, the absolute length of both fault segments for each subevent depends on the assumed rupture speed, and is not constrained well. The optimum rupture lengths are $L1=100$ km, $L2=40$ km for source I and $L1=60$ km, $L2=40$ km for source II. On the other hand, the fault orientation is relatively well established here since modification of the rupture azimuth for either of the two subfaults clearly affects the predicted radiation patterns (cf. Figs. S17 and S18 in the Supplementary material). This result is consistent with the aftershock distribution (cf. Fig. 1 and Fig. S3 in the Supplementary material), which suggests that slip was dominated by rupture on two subparallel WNW–ESE faults.

The partitioning of the rupture into distinct subevents can also be observed at shorter periods. We computed stacks of P-wave coda envelopes in the 0.7–5 s passband for epicentral distances of 30–95°. All vertical component traces within this epicentral distance range are corrected for the instrument response and bandpass filtered between 0.7 s and 5 s. The corresponding envelopes are then aligned with respect to the P wave arrival and stacked in azimuth bins of 10°. All stacks of less than 3 channels are rejected. As shown in Fig. 9c, a discrete phase can be easily tracked around 100 s after the P wave arrival for different station azimuths. This is in good agreement with the timing of the second subevent.

Meng et al. (2012) also performed back-projections of short period (1–2 s) P waves from the Japanese Hi-Net network and European networks using the MUSIC technique. The backprojection images and their interpretation are not the main purpose of the current study and they are referenced here for comparison with our long-period observations. The results obtained by Meng et al. (2012) are presented in Fig. 9a and b. There is an overall good agreement between the spatio-temporal positions of high-frequency radiation peaks and the proposed two-subevent model. From back-projection images, Meng et al. (2012) proposed the following complex rupture process presented in the inset scheme in Fig. 9a. The rupture initiated on a WNW–ESE fault (fault A) within the first 25 s after the origin time, followed by a NNE–SSW bilateral rupture (fault B) up to 80 s after the origin time. This was followed by a rupture along a second WNW–ESE fault (fault C) located about 150 km south of the first fault (fault A). This stage lasts until 150 s after origin time when rupture ends on a parallel WNW–ESE fault (fault D) close to the Ninetyeast ridge. Besides the clear pulse around 100 s visible on stacks of P-wave coda envelopes (Fig. 9c), we also see other discrete, but less coherent phases around 60 s and 180 s after the P arrival time which may be related to the intermediate rupture on fault B and to the late WNW–ESE faulting on fault D. However, the intermediate rupture on fault B and the late rupture on fault D are not obvious in our

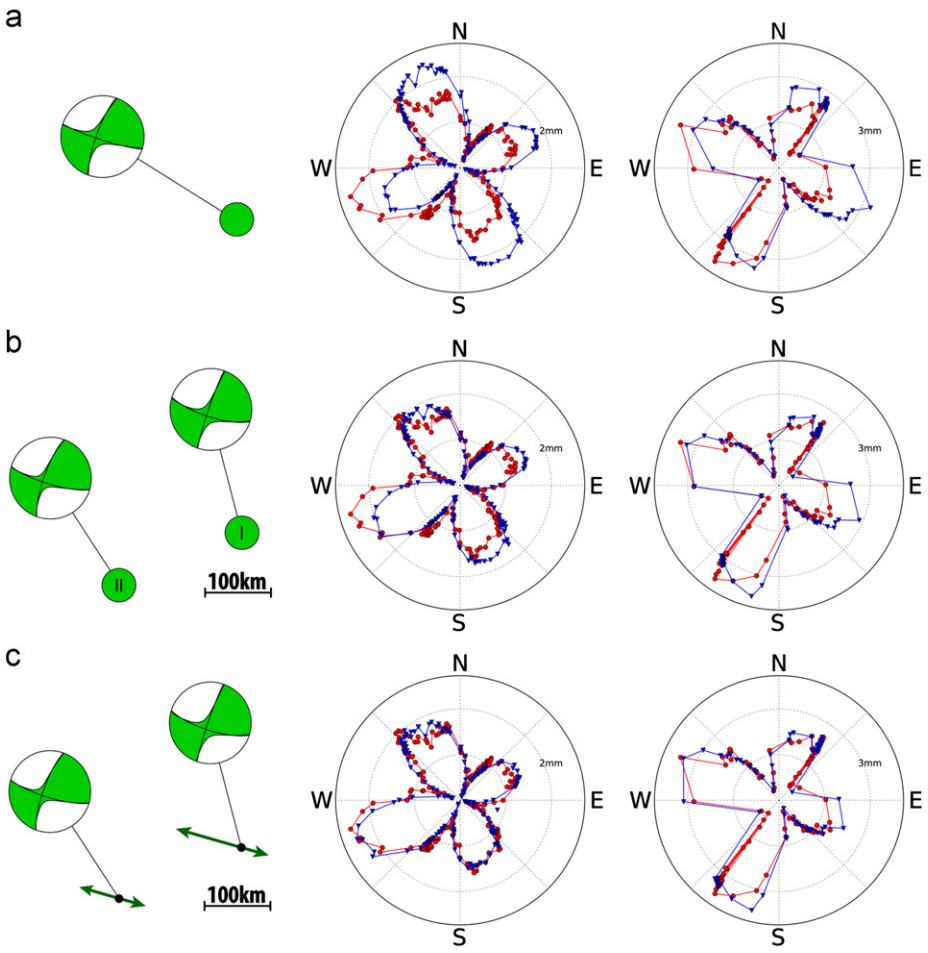

Fig. 6. Comparison of observed and predicted surface-wave radiation patterns for three simple rupture models. Comparison of observed (red circles) and predicted (blue triangles) equalized amplitudes for Rayleigh R1, R2 (middle) and Love G1, G2 (right). (a) Single-point-source model. (b) Two-point-source model. (c) Optimum source model assuming uniform slip and horizontal rupture propagation: two parallel WNW–ESE bilateral ruptures with significant directivity in the WNW direction. (For interpretation of the references to color in this figure legend, the reader is referred to the web version of this article.)

long period results. We performed 3-point-source inversions using different frequency bands (i.e., 120–400 s, 150–500 s and 200–500 s) but they did not provide stable results, with the optimum location of the two later subevents being randomly distributed in time and space. This could be explained if the high-frequency radiators on faults B and D did not involve large amounts of slip compared to WNW–ESE faulting on faults A and C; such disparity between short-period and long-period radiation has already been observed for large megathrust earthquakes such as the Mw=9.0 2011 Tohoku-oki earthquake (Meng et al., 2012), the Mw=8.8 2010 Maule Chile earthquake (Kiser and Ishii, 2011) and the Mw=9.1 2004 Sumatra earthquake (Lay et al., 2012). This assumption is compatible with the finite-fault model proposed by Yue et al. (in press) which suggests that the two main slip contributions are associated with faults A and C, with smaller slip being associated with faults B and D. Although the focal mechanism on the intermediate NNE–SSW fault (fault B) is still a matter of debate, the surface-wave radiation pattern for the whole rupture shows very clear and deep nodes (Figs. 2 and 6) which rules out any significant thrust or normal subevents.

8. Discussion and conclusion

Various seismological observations from high-frequency P waves to long-period surface waves reveal a remarkable complexity in the early stages of the 2012 Sumatra earthquake sequence. Our analysis of long-period seismic waves yielded a two-point-source model for the Mw=8.6 mainshock. The first subevent has a magnitude of Mw=8.5 with a centroid time of 36 s after the origin time. The second subevent has a magnitude of Mw=8.3 with a centroid time of 106 s after the origin time. The best-fit centroid depth is 30 km for both subevents. This two-point-source model is currently the most robust zeroth-order model that can explain the overall asymmetry of long-period (100–400 s) Rayleigh and Love wave radiation patterns for the Mw=8.6 mainshock.

To explain the remaining discrepancy in the radiation patterns, we can invoke a simple asymmetric bilateral rupture for both the first and the second subevents. This model with simple parameterization involves two parallel WNW–ESE faults separated by about 150 km, shown in Fig. 6c. This interpretation of a dominant slip contribution from two parallel WNW–ESE faults is compatible with the MRF back-projection and with the slip model proposed by Yue et al. (in press). Such fault orientations have been previously observed on multibeam bathymetry and seismic reflection profiles along the Ninetyeast Ridge (Sager et al., 2010; Meng et al., 2012) and are in good agreement with the distribution of aftershocks, which highlight two clear parallel WNW–ESE trends. These WNW–ESE oriented ruptures are also very consistent with the predicted motion of the Australian Plate relative to the Indian Plate of about 13 mm/yr in the direction of 316°N (white arrows in Fig. 1, DeMets et al., 2010).

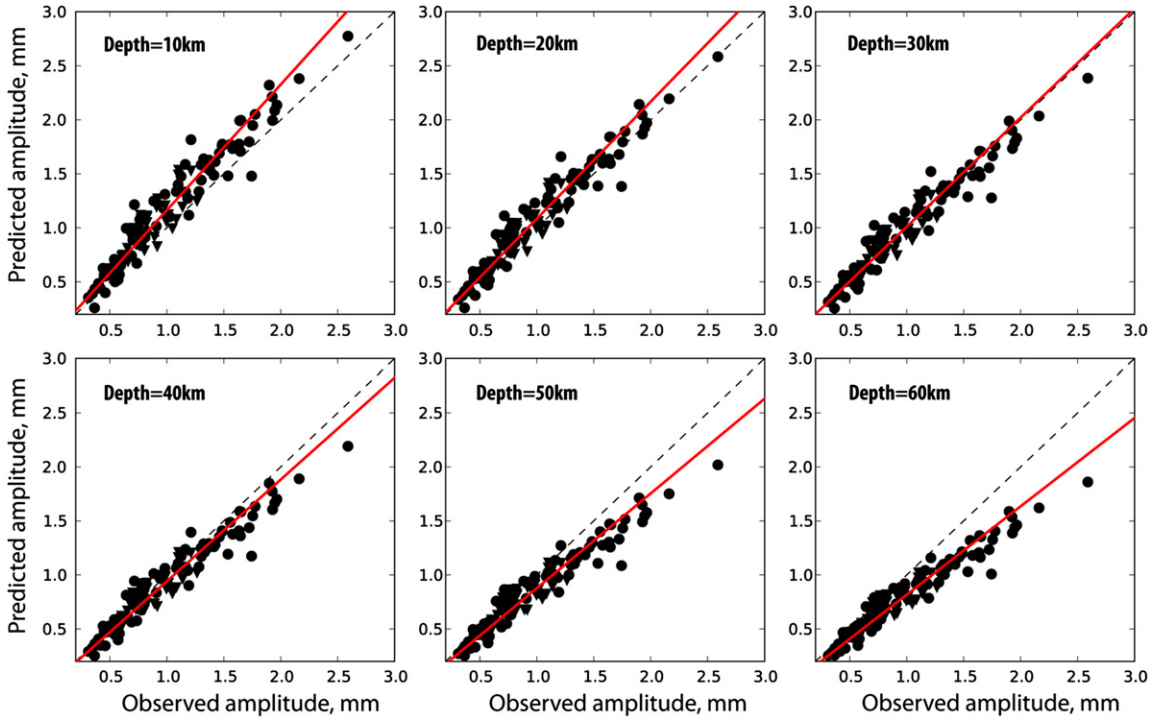

Fig. 7. Comparison between observed and predicted long-period Rayleigh wave amplitudes for the Mw=8.6 mainshock at different centroid depths. The amplitudes are measured in the 200–600 s passband and predicted amplitudes are computed for the two-point-source model presented in Section 5. Black circles and triangles indicate the rms amplitudes measured for R1 and R2, respectively. The corresponding least-square best-fit line is shown in solid lines and the 1:1 relationship between data and synthetics is shown with a dashed line.

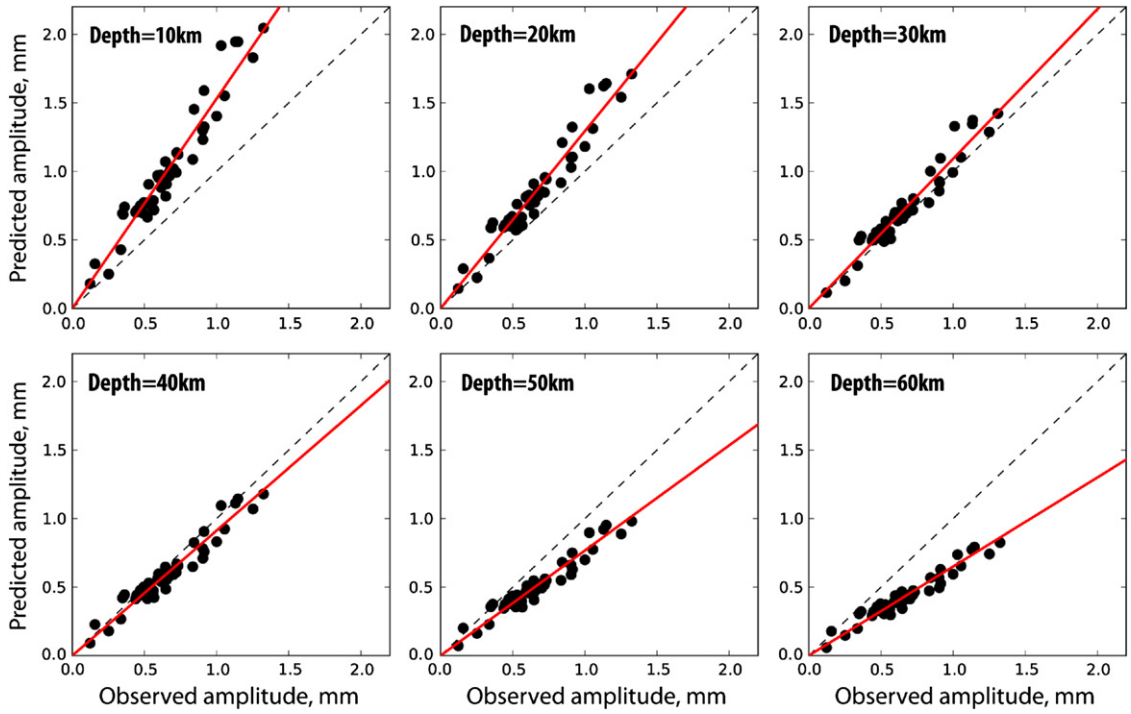

Fig. 8. Comparison between observed and predicted long-period Rayleigh wave amplitudes for the Mw=8.2 aftershock at different centroid depths. The amplitudes are measured in the 100–400 s passband and predicted amplitudes are computed for the single-point-source model presented in Section 2. Black circles indicate the rms amplitudes measured at each station. The corresponding least-square best-fit line is shown in solid lines and the 1:1 relationship between data and synthetics is shown with a dashed line.

From the relative centroid locations we obtained for the Mw=8.6 mainshock and the Mw=8.2 aftershock, and from the NNE–SSW lineations of the fracture zones in the Cocos Basin, one might theorize that the main rupture would have occurred on a fault with a similar NNE–SSW orientation. Moreover, most historic events in this region have been previously interpreted as slip on NNE–SSW striking faults. The dominant rupture on WNW–ESE faults thus brings a new perspective on the seismotectonics of

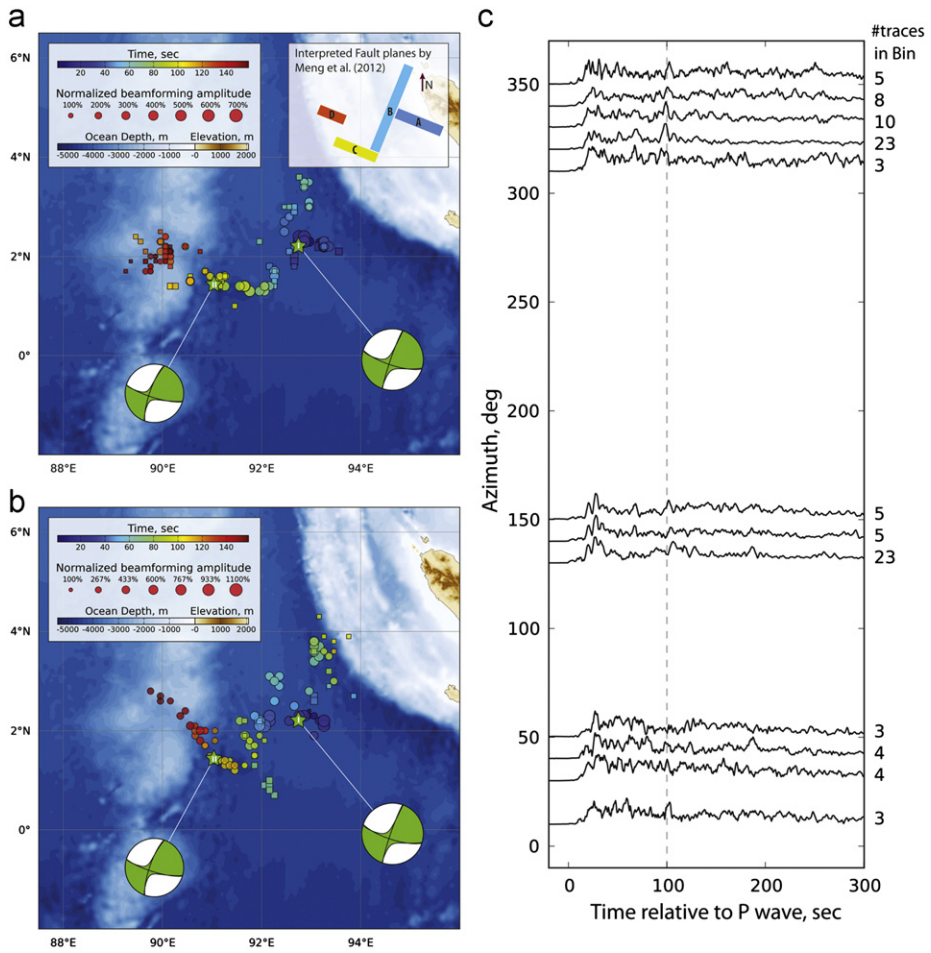

Fig. 9. High-frequency observations during the Mw=8.6 2012 Sumatra earthquake. High-frequency source imaging results of the Mw=8.6 Sumatra earthquake were obtained by Meng et al. (2012). (a) Back-projection results obtained using European networks. (b) Back-projection results obtained using the Hi-Net Japanese network. Colored circles and squares indicate, respectively, the position of primary and secondary peaks of high-frequency radiation. The two-point-source model obtained in the present study is indicated for comparison (green mechanisms and stars labeled I and II). The upper right inset in a shows the interpreted fault planes proposed by Meng et al. (2012). (c) P wave coda stacks between 30° and 95° of epicentral distance. Only stacks with more than 3 traces are depicted. The gray dashed line indicates a discrete phase which is visible at different azimuths approximately 100 s after the P wave arrival. (For interpretation of the references to color in this figure legend, the reader is referred to the web version of this article.)

the diffuse Indo-Australian plate boundary. This would not be the first time a major intraplate earthquake has ruptured at high angle to the existing fracture zones. The Mw=8.1 1998 Balleny Islands earthquake stands as a good example for this (Hjörleifsdóttir et al., 2009). Satriano et al. (in press), however, proposes a different interpretation involving several sequential NNE–SSW ruptures. Their interpretation does not seem to be compatible with our refined model involving two subevents that have strong directivity toward the WNW. The back-projection results presented by Satriano et al. (in press) are not, however, inconsistent with our results. This is particularly true for their high-resolution image obtained with a passband of 0.5–1.0 Hz, which is in very good agreement with our most robust two-point-source model. We do not exclude such complicated models involving (possibly orthogonal) NNE–SSW faults, as long as these ruptures do not violate the constraints from long-period waves (i.e., scalar seismic moment, surface wave radiation pattern and the overall westward directivity). If more complex rupture models are preferred from other data sets, such as very high-frequency P waves and teleseismic body waves, these models can be tested against the long-period data presented here, especially the surface-wave radiation patterns, shown in Fig. 6c.

The Mw=8.6 mainshock was followed two hours later by a Mw=8.2 aftershock, which occurred approximately 200 km to the south. To analyze the source of this major aftershock, we subtracted the SEM synthetics for the Mw=8.6 mainshock from the data and used the corresponding residuals as the data vector. This was done to clean up the seismograms from large amplitude disturbances due to the surface-wave arrivals of the Mw=8.6 mainshock. The focal mechanism obtained for the Mw=8.2 aftershock shows a very small non-double-couple component. This result as well as the surface-wave radiation diagram suggest a simpler rupture than the Mw=8.6 mainshock. This is in good agreement with backprojection results that indicates a simple bilateral rupture along a NNE–SSW fault (Meng et al., 2012).

Our analysis of the surface-wave amplitudes points out a large centroid depth ($h_c \sim 30$ km) both for the Mw=8.6 mainshock and the Mw=8.2 aftershock. This indicates a relatively large depth extent of faulting. If we consider the simple case of uniform slip with depth up to the seafloor, the depth extent of faulting would be as much as 60 km (i.e., $2h_c$, assuming negligible variation of the shear modulus as a function of depth), so that the slip potency above and below the centroid is equal. If the slip linearly decreased with depth, then the depth extent could be as much as 90 km (i.e., $3h_c$). The latter is more consistent with several finite-fault inversion results for the Mw=8.6 mainshock which indicate fairly large slip at shallow depths (Hayes, 2012; Shao et al., 2012; Wei, 2012; Yue et al., in press). In any case, the Mw=8.6 and Mw=8.2 2012 Sumatra earthquakes most likely

involved substantial lithospheric deformation that may eventually lead to the formation of a localized plate boundary.

Acknowledgments

We thank Shengji Wei, Don Helmberger, Thorne Lay and two anonymous reviewers for helpful discussions. This work uses Federation of Digital Seismic Networks (FDSN) seismic data and CMT solutions from the Global CMT catalog. The Incorporated Research Institutions for Seismology (IRIS) Data Management System (DMS) was used to access the data. This work made use of the Matplotlib python library, of the Basemap toolkit and of the neighbourhood algorithm sampler developed by Malcolm Sambridge. Lingsen Meng and Jean-Paul Ampuero were supported by NSF Grant EAR-1015704.

Appendix A. Supporting information

Supplementary data associated with this article can be found in the online version at doi:10.1016/j.epsl.2012.07.017.

References

Ammon, C.J., Velasco, A.A., Lay, T., 2006. Rapid estimation of first-order rupture characteristics for large earthquakes using surface waves: 2004 Sumatra–Andaman earthquake. Geophys. Res. Lett. 33, L14314.

Bassin, C., Laske, G., Masters, G., 2000. The current limits of resolution for surface wave tomography in North America. Eos Trans. AGU 81.

Ben-Menahem, A., 1961. Radiation of seismic surface-waves from finite moving sources. Bull. Seismol. Soc. Am. 51, 401–435.

Ben-Menahem, A., Aboodi, E., Schild, R., 1974. The source of the great Assam earthquake—an interplate wedge motion. Phys. Earth Planet. Inter. 9, 265–289.

Bertero, M., Bindi, D., Boccacci, P., Cattaneo, M., Eva, C., Lanza, V., 1999. Application of the projected Landweber method to the estimation of the source time function in seismology. Inverse Probl. 13, 465–486.

Chen, W., Molnar, P., 1977. Seismic moments of major earthquakes and the average rate of slip in central Asia. J. Geophys. Res. 82, 2945–2969.

Delescluse, M., Chamot-Rooke, N., 2007. Instantaneous deformation and kinematics of the India–Australia Plate. Geophys. J. Int. 168, 818–842.

DeMets, C., Gordon, R.G., Argus, D.F., 2010. Geologically current plate motions. Geophys. J. Int. 181, 1–80.

Deplus, C., Diament, M., Hébert, H., Bertrand, G., Dominguez, S., Dubois, J., Malod, J., Patriat, P., Pontoise, B., Sibilla, J.-J., 1998. Direct evidence of active deformation in the eastern Indian oceanic plate. Geology 26, 131–134.

Duputel, Z., Rivera, L., Kanamori, H., Hayes, G., 2012. W phase source inversion for moderate to large earthquakes (1990–2010). Geophys. J. Int. 189, 1125–1147.

Duputel, Z., Rivera, L., Kanamori, H., Hayes, G.P., Hirshorn, B., Weinstein, S., 2011. Real-time W Phase inversion during the 2011 off the Pacific Coast of Tohoku Earthquake. Earth Planets Space 63, 535–539.

Dziewonski, A.M., Anderson, D.L., 1981. Preliminary reference Earth model. Phys. Earth Planet. Inter. 25, 297–356.

Ekström, G., Nettles, M., Dziewonski, A.M., 2012. The global CMT project 2004-2010: centroid-moment tensors for 13,017 earthquakes. Phys. Earth. Planet. Inter. 200–201, 1–9.

Haskell, N.A., 1963. Radiation pattern of Rayleigh waves from a fault of arbitrary dip and direction of motion in a homogeneous medium. Bull. Seismol. Soc. Am. 53, 619–642.

Hauksson, E., Stock, J., Hutton, K., Yang, W., Vidal-Villegas, J.A., Kanamori, H., 2011. The 2010 Mw 7.2 El Mayor–Cucapah Earthquake Sequence, Baja California, Mexico and Southernmost California, USA: active seismotectonics along the Mexican Pacific Margin. Pure Appl. Geophys. 168, 1255–1277.

Hayes, G.P., 2012. USGS Finite Fault Model for the Mw=8.6 Earthquake off the West Coast of Northern Sumatra. 〈http://earthquake.usgs.gov/earthquakes/eqinthenews/2012/usc000905e/finite_fault.php〉.

Hayes, G.P., Furlong, K.P., Ammon, C.J., 2009a. Intraplate deformation adjacent to the Macquarie Ridge south of New Zealand—the tectonic evolution of a complex plate boundary. Tectonophysics 463, 1–14.

Hayes, G.P., Rivera, L., Kanamori, H., 2009b. Source inversion of the W-Phase: real-time implementation and extension to low magnitudes. Seismol. Res. Lett. 80, 817–822.

Henry, C., Das, S., Woodhouse, J.H., 2000. The great March 25, 1998, Antarctic Plate earthquake: moment tensor and rupture history. J. Geophys. Res. 105, 16097–16118.

Hjörleifsdóttir, V., Kanamori, H., Tromp, J., 2009. Modeling 3-D wave propagation and finite slip for the 1998 Balleny Islands earthquake. J. Geophys. Res. 114, B03301.

Kanamori, H., 1970. Synthesis of long-period surface waves and its application to earthquake source studies—Kurile Islands earthquake of October 13, 1963. J. Geophys. Res. 75, 5011–5027.

Kanamori, H., 1993. W phase. Geophys. Res. Lett. 20, 1691–1694.

Kanamori, H., Rivera, L., 2008. Source inversion of W phase: speeding up seismic tsunami warning. Geophys. J. Int. 175, 222–238.

Kiser, E., Ishii, M., 2011. The 2010 Mw 8.8 Chile earthquake: triggering on multiple segments and frequency-dependent rupture behavior. Geophys. Res. Lett. 38, L07301.

Kiser, E., Ishii, M., 2012. Preliminary Rupture Modelling of the April 11, 2012 Sumatran Earthquakes. 〈http://www.seismology.harvard.edu/research_sumatra2012.html〉.

Komatitsch, D., Tromp, J., 1999. Introduction to the spectral element method for three-dimensional seismic wave propagation. Geophys. J. Int. 139, 806–822.

Kustowski, B., Ekström, G., Dziewonski, A.M., 2008. Anisotropic shear-wave velocity structure of the Earth's mantle: a global model. J. Geophys. Res. 113, B06306.

Lanza, V., Spallarossa, D., Cattaneo, M., Bindi, D., Augliera, P., 1999. Source parameters of small events using constrained deconvolution with empirical Green's functions. Geophys. J. Int. 137, 651–662.

Lay, T., Kanamori, H., Ammon, C.J., Koper, K.D., Hutko, A.R., Ye, L., Yue, H., Rushing, T.M., 2012. Depth-varying rupture properties of subduction zone megathrust faults. J. Geophys. Res. 117, B04311.

Meng, L., Ampuero, J.-P., Stock, J., Duputel, Z., Luo, Y., Tsai, V.C., 2012. An earthquake in a maze: compressional rupture branching during the April 11 2012 M8.6 Sumatra earthquake. Science 337 (6095), 724–726.

Meng, L., Inbal, A., Ampuero, J.-P., 2011. A window into the complexity of the dynamic rupture of the 2011 Mw 9 Tohoku-Oki earthquake. Geophys. Res. Lett. 38, L00G07.

Okal, E.A., 1977. The July 9 and 23, 1905, Mongolian earthquakes: a surface wave investigation. Earth Planet Sci. Lett. 34, 326–331.

Ruff, L.J., 1984. Tomographic imaging of the earthquake rupture process. Geophys. Res. Lett. 11, 629–632.

Sager, W.W., Paul, C.F., Krishna, K.S., Pringle, M., Eisin, A.E., Frey, F.A., Gopala Rao, D., Levchenko, O., 2010. Large fault fabric of the Ninetyeast Ridge implies near-spreading ridge formation. Geophys. Res. Lett. 37, L17304.

Sambridge, M., 1999. Geophysical inversion with a neighbourhood algorithm—I. Searching a parameter space. Geophys. J. Int. 138, 479–494.

Satriano, C., Kiraly, E., Bernard, P., Vilotte, J.-P. The 2012 Mw 8.6 Sumatra earthquake: evidence of westward sequential seismic ruptures associated to the reactivation of a N–S ocean fabric. Geophys. Res. Lett. in press. http://dx.doi.org/10.1029/2012GL052387.

Schlupp, A., Cisternas, A., 2007. Source history of the 1905 great Mongolian earthquakes (Tsetserleg, Bolnay). Geophys. J. Int. 169, 1115–1131.

Shao, G., Li, X., Ji, C., 2012. Preliminary Result of the April 11, 2012, Mw 8.64 Sumatra Earthquake. 〈http://www.geol.ucsb.edu/faculty/ji/big_earthquakes/2012/04/10/sumatra.html〉.

Tocheport, A., Rivera, L., Van der Woerd, J., 2006. A study of the 14 November 2001 Kokoxili Earthquake: history and geometry of the rupture from teleseismic data and field observations. Bull. Seismol. Soc. Am. 96, 1729–1741.

Tsai, V.C., Hayes, G.P., Duputel, Z., 2011. Constraints on the long-period moment-dip tradeoff for the Tohoku earthquake. Geophys. Res. Lett. 38, L00G17.

Tsuboi, S., Komatitsch, D., Ji, C., Tromp, J., 2003. Broadband modeling of the 2002 Denali fault earthquake on the Earth Simulator. Phys. Earth Planet. Inter. 139, 305–313.

Wei, S., 2012. Tectonic Observatory Source Models of Large Earthquakes—April/11/2012 (Mw 8.6), Sumatra. 〈http://www.tectonics.caltech.edu/slip_history/2012_Sumatra/index.html〉.

Wiens, D., DeMets, C., Gordon, R., Stein, S., Argus, D., Engeln, J.F., Lundgren, P., Quible, D., Stein, C., Weinstein, S., Woods, D.F., 1985. A diffuse plate boundary model for Indian Ocean tectonics. Geophys. Res. Lett. 12, 429–432.

Yue, H., Lay, T., Koper, K.D. The Great Intraplate Earthquakes of 11 April 2012: En Echelon and conjugate fault ruptures on an emerging Indian–Australian Plate Boundary. Nature, http://dx.doi.org/10.1038/nature11492, in press.